European Journal of Sustainable Development Research
2025, 9(2), em0282
e-ISSN: 2542-4742
https://www.ejosdr.com/

MODESTUM

Research Article

OPEN ACCESS

Assessment of 10-kW swept-bladed horizontal axis wind turbines performance by modified blade element momentum method

Kamal Abdel Radi Ismail [1], Pedro Antonio Assad Baracat [1,2*]

[1] Department of Energy, Faculty of Mechanical Engineering, State University of Campinas, Campinas/SP, BRAZIL
[2] Fundação para Inovações Tecnológicas (FITec), Campinas/SP, BRAZIL
***Corresponding Author:** pedroaab@gmail.com

Citation: Ismail, K. A. R., & Baracat, P. A. A. (2025). Assessment of 10-kW swept-bladed horizontal axis wind turbines performance by modified blade element momentum method. *European Journal of Sustainable Development Research, 9*(2), em0282. https://doi.org/10.29333/ejosdr/16053

ARTICLE INFO

Received: 03 Nov. 2024

Accepted: 11 Feb. 2025

ABSTRACT

In this work, a modified blade element momentum algorithm of low computational cost was written in MATLAB, to analyze the concept of swept blade horizontal axis wind turbine. The algorithm was validated by comparing the numerical predictions with results available in the literature. Different geometrical arrangements of 10-kW horizontal axis wind turbines with Göttingen airfoils (GOEs) with different maximum thickness and camber to chord ratios and tip sweep angles were designed and compared. The influence of maximum thickness and camber to chord ratios, as well as the blade tip sweep angle over the power generation, torque and thrust of horizontal axis wind turbines were evaluated. The torque and thrust distributions as well as the contributions of the different regions of the blades to power generation were also assessed. Results showed that high maximum thickness to chord ratio and moderate maximum chamber to chord ratio increase power generation. For horizontal axis wind turbines using GOE 413 airfoil with tip speed ratio (TSR) equal to 8, the tip sweep angle of 40° resulted in a power generation of 10,669.81 W and a thrust of 1,776.89 N, which are 6.16% higher and 31.32% lower than the straight blade case, respectively. Also, it was found that the thrust generated in the backward swept blade regions is lower than the cases of straight blade and forward swept blade. The results confirm the adequacy of backward sweep blades for horizontal axis wind turbine rotors for TSR equal to 8 at a wind velocity of 9 m/s, due to the power generation increase and thrust reduction. Also, the results confirm that backward swept blades are appropriate for high size rotors, due to the thrust reduction, which reduces the structural deformation.

Keywords: swept blades, horizontal axis wind turbine, power coefficient, thickness/chord ratio, chamber/chord ratio, Göttingen airfoils

INTRODUCTION

The use of renewable energy sources is growing rapidly around the world, including wind energy. However, there is an increasing need for alternative energy sources to match traditional sources in terms of viability and financial return. In countries such as United States of America, the past research on wind energy generated positive economic returns (Wiser & Millstein, 2020). The cost of energy (CoE) from wind power has seen a huge drop, and it is cheaper than the energy generated in existing coal and gas plants (Gözcü et al., 2022). Global wind energy installed capacity showed a high growth in the past decades, from 18 GW in 2000, to 590 GW in 2019 (Dorrell & Lee, 2020).

Ancient Egyptians were the first to use the wind power, to sail their boats, around 5000 B.C. After that, windmills were used in Iran to grind grains. Centuries later, the windmill basic concept was applied in the Netherlands (Khandakar & Kashem, 2020). The first electricity-generating wind turbine was created by James Blyth, in 1887 (Sharma et al., 2022).

There are two main types of wind turbines: horizontal axis wind turbines (HAWTs) and vertical axis wind turbines (VAWTs). The rotation axis of a HAWT is parallel to the wind direction, while the rotation axis of a VAWT is perpendicular to the wind direction (Ahmad et al., 2020). For low wind velocities and disturbed or turbulent flows, VAWTs have advantages over HAWTs. Also, VAWTs can receive winds from any direction, and they produce less noise than HAWTs, which is ideal for urban areas (Johari et al., 2018). However, HAWTs are more efficient in wind energy conversion, and they are used for large power generation, as the 4.8 MW GE turbine (Liu et al., 2019).

Small-medium-sized HAWTs are also being applied in urban and isolated rural areas. Between 2013 and 2018, the cumulative installed capacity of small HAWTs showed a growth of 50%, achieving 1,727 MW in 2018. Unlike large multi-MW HAWTs, designed to operate under optimal conditions, small HAWTs can be designed for operating in a

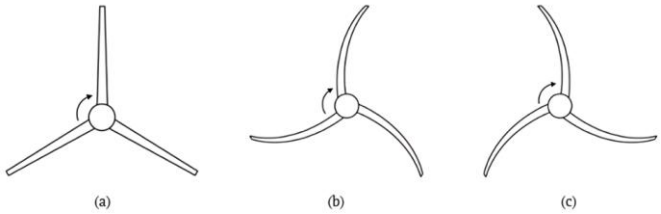

Figure 1. Different HAWT geometries representations: (a) Straight bladed HAWT, (b) Forward swept bladed HAWT, & (c) Backward swept bladed HAWT (Source: Authors' own elaboration)

broad range of wind conditions, including low wind velocities, and present good start-up performances (Gözcü et al., 2022).

The challenges for a good use of wind resources include the increase of the power coefficient (C_p) of wind turbines. The C_p represents the overall efficiency of a wind turbine, which is the ratio between the output power and the total power associated to the wind (Hernández & Cabrera, 2018). According to Betz, the theoretical maximum C_p that can be reached by any wind turbine is $16/27 \cong 0.59$ (Fadil et al., 2017). HAWTs present the highest C_p values, compared to VAWTs. While HAWTs can reach a C_p of 0.5, the maximum C_p of VAWTs is around 0.4. HAWTs produce around 85% of total wind power generation (Redchyts et al., 2023), as most wind turbines in operation are of the horizontal axis type (Kamran, 2022).

According to Fritz et al. (2024), wind turbine rotors with straight blades are becoming increasingly large, in the pursuit of reducing the levelized CoE. Consequently, wind turbine blades become more flexible, increasing the interaction between aerodynamic forces and structural deformations. Swept-bladed HAWTs, on the other hand, allows the increase of the blade length (to capture more power from the wind) without increasing the rotor radius, besides reducing aerodynamic noise. Despite the more complex geometry of swept-bladed HAWTs, it has a good potential for load alleviation (Li et al., 2022; Pavese et al., 2017) and for increasing the power generation and the C_p, compared to HAWTs with straight blades (Larwood et al., 2014). However, more studies on this type of geometry are necessary for a complete characterization of its advantages (Kaya et al., 2018). Straight and swept-bladed HAWTs geometries are represented in **Figure 1**. For the swept-bladed HAWTs of **Figure 1**, the sweep angle starts in 0°, from the blade root until the tip.

Gözcü et al. (2022) carried out dynamic investigations of 100-kW straight-bladed and swept-bladed HAWTs, by performing modal analysis, dynamic load analysis and flutter analysis. Their results showed that passive load mechanisms (aeroelastic tailoring) can reduce the loads over the blades, without compromising performance.

Sessarego et al. (2018) have analyzed the wake including complex inflow conditions (turbulent wind and extreme shear) of HAWTs' blades with winglets and sweep through vortex-based codes and compared the effect of sweep and winglets to straight blades. They concluded that blades with sweep or winglets may present better performance, compared to their straight blade counterparts.

Li et al. (2020) proposed a method for including curved bound vortex influence at HAWT's blades. According to the authors, in order to calculate the load distribution along swept blades, it is necessary to evaluate the influence of the curved shape on the blade's aerodynamics, especially for blades designed with aeroelastic tailoring (Scott et al., 2017).

Veloso et al. (2023) investigated the effects of swept blades on the starting and operational performance of small HAWTs. They evaluated the influence of swept-blade angle over aerodynamic torque and thrust force, and the required wind velocity for starting a small HAWT. According to their results, swept blades may not reduce the thrust or increase the torque, depending on operation conditions. The authors stated that the thrust reduction and the torque increase caused by swept blades also depend on the airfoil used.

Verelst and Larsen (2010) investigated 120 different swept blade configurations (forward and backward sweep). Their results for backward sweep showed lower blade root flap-wise fatigue and extreme loads, as well as reduced loading on shaft and tower. On the other hand, forward sweeps increased fatigue and extreme loads.

Khalafallah et al. (2019) have analyzed the influence of winglets on the performance of swept-bladed HAWTs, through computational fluid dynamics (CFD) simulations. They concluded that winglets and sweep can increase power generation. The highest improvement in C_p was of 4.39% at the design tip speed ratio (TSR) of 6.

According to Larwood et al. (2014), the blade sweep permits increasing the rotor diameter to capture more power. They described a study of swept blade design parameters for 750-kW HAWT. They also conducted a design study to implement a swept design on 1.5-MW, 3-MW, and 5-MW HAWTs, aiming a 5% increase in annual energy production over the straight blade, without increasing blade loads. This goal was achieved for the 1.5-MW and 3-MW HAWTs. Also, their results showed that loads and energy production were the most sensitive parameters to the tip sweep.

Horcas et al. (2023) described different state-of-the-art computational aerodynamic models for the design stage of curved tip extensions of HAWTs: a blade-resolved navier stokes solver, a lifting line model, a vortex-based method coupling a near-wake model with a far-wake model, and two implementations of blade element momentum (BEM), with and without radial induction. All methods showed noticeable differences of thrust and power from CFD, for the baseline configuration. The methods showed similar results when assessing the impact of different tip shapes over the thrust. CFD showed different results when assessing the impact of different tip shapes over the power. BEM results were different from other methods when predicting the impact of different blade tip shapes over the blade sectional load.

Fritz et al. (2022) proposed a correction model that enables the extension of BEM for swept blades. The proposed extension corrects the axial induction regarding the azimuthal displacement of the trailed vorticity system and the induction of the curved bound vortex on itself.

Fritz et al. (2024) performed an experimental analysis of a HAWT with aft-swept blades using particle image velocimetry in a wind tunnel. Their results provide a comprehensive aerodynamics characterization of rotating swept blades in controlled conditions and can be used in the validation of

higher-fidelity models, such as CFD, and lower-fidelity models, such as BEM. The blade sweep model applied in this study can be considered polynomial, since the swept blades are derived from a straight reference with a displacement as a function of the radial position and other parameters raised to the power of 2. Barlas et al. (2021) also performed wind tunnel analysis of a HAWT swept blade. They concluded that experimental and CFD results showed good agreement in terms of flow visualization and pressure distribution.

Pholdee et al. (2023) presented an optimal design of swept blade for HAWTs using a hybrid surrogate-assisted optimizer. The goal was to maximize the ratio of the torque coefficient to the thrust coefficient of a HAWT at a wind velocity of 10 m/s. CFD was used for the aerodynamic analysis of the wind turbine blade. According to the authors, their proposed model of analysis is the most efficient for the sweep blade design problem. The optimal blade design improved the torque, thrust and the ratio of the torque coefficient to the thrust coefficient by approximately 31.0%, 18.7%, and 15% from the original design, respectively.

From the momentum conservation and the actuator disk (AD) method, it is possible to optimize aspects of the geometry of HAWTs. In this work, the AD method and a modified BEM method for swept blades were used as a low computational cost algorithm in MATLAB. The lift (C_l) and drag (C_d) coefficients are possible inputs of this algorithm, and were provided from different sources, for comparison purposes. One source was the literature, from which tables of C_l and C_d were made to be read during the algorithm's execution. The other source was an interface between the modified BEM code and XFoil (Drela, 2013).

The modified BEM code was used to optimize and analyze different concepts of swept-bladed 10-kW HAWTs and its correspondents straight-bladed HAWTs, with Göttingen airfoils, which are widely used for wind energy. The sweep angle at the blade root was kept at 0°, and different tip sweep angles were analyzed, to assess the influence of the airfoil maximum thickness (t) and camber (z), and the blades sweep geometry over the power and C_p curves with TSR. Based on the literature revision, this is the first detailed study on those airfoils characteristics in swept-bladed HAWTs. Also, the contribution of different sectors of the blades to torque/power generation and thrust were analyzed through the torque distribution along the blades.

The present work investigating wind energy methods to improve their production and provide more energy is in line with the objectives of the United Nations sustainable developments goals promoting clean and accessible energy (SDG7 affordable and clean energy).

The literature review shows little information on swept blade horizontal axis wind turbines especially in relation to performance parameters and experimental and numerical results. The main contribution of the present study is to provide a detailed numerical evaluation of the aerodynamic and performance parameters in comparison with straight blade wind turbines, besides showing that swept blades can increase torque, reduce axial thrust loads and aerodynamic noise making it suitable for urban applications on top of buildings and residential condominium.

THEORETICAL ASPECTS

Optimization of Straight-Bladed HAWT Geometry

The AD theory assumes that the momentum rate of change of the flow within the stream-tube is equal to the momentum rate of change of the AD. The momentum rate of change is due to the pressure difference over the AD, as the stream-tube is surrounded by atmospheric pressure. From the AD theory, the power coefficient for straight-bladed HAWTs can be derived, as in Eq. (1) (Burton et al., 2001):

$$C_p = \frac{2P}{\rho V_\infty^3 \pi R^2}. \quad (1)$$

In Eq. (1), P is the wind turbine power, ρ the air density, V_∞ is the free stream velocity and R is the rotor radius. In an optimum design, a maximum C_p ($C_{p,max}$) is obtained. The terms of Eq. (1) can be rearranged, for the optimum radius calculation (with maximum C_p), which gives Eq. (2):

$$R = \sqrt{\frac{2P}{\rho V_\infty^3 \pi C_{p,max}}}. \quad (2)$$

In Eq. (2), P is the expected power and R is the optimized rotor radius. From the BEM theory, $C_{p,max}$ is given by Eq. (3) (Hansen, 2008):

$$C_{p,max} = \left(1 - \frac{1.386}{B} sin\ \frac{\phi}{2}\right)^2 \frac{16}{27}\left(e^{-0.35\lambda^{-1.29}} - \frac{C_d}{C_l}\lambda\right). \quad (3)$$

In Eq. (3), λ is the tip speed ratio at the blade tip, as a function of dimensionless radius r/R (r is the local radius, or the blade element radius), B is the number of blades and ϕ is the angle between the plane of rotation and the flow relative velocity, as a function of λ, for the angle of attack (α) that gives the maximum value of C_l/C_d (α_{opt}). The same values of C_l and C_d are used in Eq. (3).

The first step to optimize the blade's geometry of a straight-bladed HAWT is to define an airfoil to be used in the blades, a TSR value and an expected output power. From the chosen airfoil, C_l, C_d, and α_{opt} for the maximum value of C_l/C_d can be found and applied to Eq. (3) and Eq. (2), in that order.

The chord $c(r)$ and twist $\theta(r)$ distributions can be optimized as well. From BEM theory, the axial induction factor (a) and the tangential induction factor (b) define the change in the flow velocity after crossing the AD. The optimum values of induction factors are $a = 1/3$ and $b = 0$. From those values, the equation for ϕ at each section of an ideal wind turbine is (Manwell et al., 2009):

$$\phi = tan^{-1}\left(\frac{2}{3\lambda}\right). \quad (4)$$

From Eq. (4), the optimum twist distribution, θ_{opt}, can be derived:

$$\theta_{opt} = \phi - \alpha_{opt}. \quad (5)$$

The optimum chord distribution along the blade m (c) is given by Eq. (6) (Manwell et al., 2009):

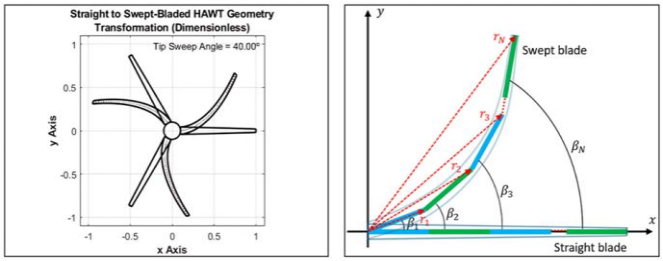

(a) (b)

Figure 2. Straight to swept blade transform: (a) Rotor geometry & (b) Blade geometry (Source: Authors' own elaboration)

$$c = \frac{8\pi r\, sin\phi}{3BC_l\lambda}. \tag{6}$$

Since the resulting non-linear curves of twist and chord along the blade may be difficult to manufacture, they can be linearized at a certain distance from the hub.

Optimization of Straight-Bladed HAWT Geometry

The function that transforms the local radius r of the straight-bladed geometry into the local radius r_j of the swept-bladed geometry is defined in Eq. (7) (Gemaque et al., 2022; Veloso et al., 2023):

$$r_j = R\left(r_{s,j}/R\right)^{\beta_j+1}, \tag{7}$$

where $r_{s,j}$ is the local radius in the blade element j of the straight-bladed HAWT, β_j is the local sweep angle in the blade element j, for a blade divided in N elements, as given by Eq. (8) (Veloso et al., 2023):

$$\beta_j = \beta_1 + (j-1)(\beta_N - \beta_1)/(N-1). \tag{8}$$

The chord length in blade element j (c_j) is given by Eq. (9) (Veloso et al., 2023):

$$c_j = c_{s,j} cos\,(\beta_j), \tag{9}$$

where $c_{s,j}$ is the chord length in the blade element j of the straight-bladed HAWT. **Figure 2** shows the straight to swept blade conversion.

Modified BEM Method to Swept-Bladed HAWTs

In each blade element j of a swept-bladed HAWT, the relation between the local angle of attack, α_j, the local twist angle, θ_j and the local angle between the plane of rotation and the relative wind velocity, ϕ_j is (Veloso et al., 2023):

$$\phi_j = \theta_j + \alpha_j. \tag{10}$$

The angle ϕ_j can be calculated with the axial induction factor for swept blade element j, a_j, the tangential induction factor for swept blade element j, b_j, the angular velocity, ω, the local radius, r_j and the local sweep angle, β_j (Veloso et al., 2023):

$$\phi_j = tan^{-1}\left[\frac{(1-a_j)V_\infty}{(1+b_j)\omega r_j cos\,(\beta_j)}\right]. \tag{11}$$

The normal ($C_{n,j}$) and tangential ($C_{t,j}$) force coefficients, used in the convergence of the values of a_j and b_j, are, respectively (Gemaque et al., 2022; Veloso et al., 2023):

$$C_{n,j} = \left[C_l\, cos(\phi_j) + C_d\, sin(\phi_j)\right] cos(\beta_j). \tag{12}$$

$$C_{t,j} = \left[C_l\, sin(\phi_j) - C_d\, cos(\phi_j)\right] cos(\beta_j). \tag{13}$$

The local relative wind velocity over the blade element j, $V_{r,j}$, is calculated through Eq. (14) (Gemaque et al., 2022; Veloso et al., 2023):

$$V_{r,j} = \sqrt{\left[V_\infty(1-a_j)\right]^2 + \left[\omega r_j cos\,(\beta_j)(1+b)\right]^2}. \tag{14}$$

With the local relative wind velocity over the blade section, it is possible to calculate the local Reynolds number (R_e), as in Eq. (15), in which μ is the dynamic viscosity of the air:

$$R_e = \frac{\rho V_{r,j} c_j}{\mu}. \tag{15}$$

$$R_e = \frac{\rho V_{r,j} c_j}{\mu} \tag{15}$$

Aerodynamic Losses, Thrust, and Torque Variations

There are some models to compute aerodynamic losses. The Prandtl tip loss factor considers the finite B. In a similar way, the hub losses can be computed through Eq. (16), Eq. (17), and Eq. (18) (Baracat et al., 2019; Gemaque et al., 2022; Hansen, 2008):

$$f_h = \frac{B(r_j - R_{hub})}{2r_j sin(\phi_j)}. \tag{16}$$

$$f_t = \frac{B(R-r_j)}{2r_j sin(\phi_j)}. \tag{17}$$

$$F = \left[(2/\pi) cos^{-1}\left(e^{f_t}\right)\right]\left[(2/\pi) cos^{-1}\left(e^{f_h}\right)\right]. \tag{18}$$

In Eq. (16), f_h is the hub loss factor and R_{hub} is the hub radius. In Eq. (17), f_t is the tip loss factor. In Eq. (18), F is the modified Prandtl's correction.

The thrust (T) and torque (Q) are calculated considering the aerodynamic losses. The thrust variation, dT/dr_j, and the torque variation, dQ/dr_j, can be calculated through Eq. (19) and Eq. (20), respectively (Kulunk & Yilmaz, 2009):

$$\frac{dT}{dr_j} = \frac{1}{2} F\rho {V_{r,j}}^2 B c_j \left[C_l\, cos(\phi_j) + C_d\, sin(\phi_j)\right]. \tag{19}$$

$$\frac{dQ}{dr_j} = \frac{1}{2} F\rho {V_{r,j}}^2 B c_j r_j \left[C_l\, sin(\phi_j) - C_d\, cos(\phi_j)\right]. \tag{20}$$

Hansen (2008) also describes Glauert and Spera corrections for calculating a_j and b_j, for high values of a_j, which were applied in the modified BEM code:

$$a_j = \begin{cases} (K+1)^{-1}, for\ a_j \le a_c \\ \frac{1}{2}\left[2 + K(1-2a_c) - \sqrt{[K(1-2a_c)+2]^2 + 4(Ka_c^2 - 1)}\right], for\ a_j > a_c \end{cases}. \tag{21}$$

$$b_j = \left\{\frac{4Fsin(\phi_j)cos\,(\phi_j)}{\sigma_j[C_l\,sin(\phi_j)-C_d\,cos(\phi_j)]}\right\}^{-1}, \quad (22)$$

where $a_c = 0.20$, σ_j is the rotor local solidity of blade element j, defined in Eq. (23) (Veloso et al., 2023), and K is defined in Eq. (24) (Hansen, 2008):

$$\sigma_j = Bc_j/(2\pi r_j). \quad (23)$$

$$K = \frac{4Fsin^2(\phi_j)}{\sigma_j[C_l\,cos(\phi_j)+C_d\,sin(\phi_j)]}. \quad (24)$$

Power Generation and Power Coefficient

From Eq. (20), the torque (Q) can be numerically calculated. The power generation (P) can be numerically calculated from the relation of Eq. (25) (Hansen, 2008):

$$dP = \omega.dQ. \quad (25)$$

The power generation can also be calculated by Eq. (26) (Hansen, 2008):

$$P = 2\rho V_\infty^3 a(1-a)^2\pi R^2. \quad (26)$$

The available power (P_{flow}) in the cross section of the stream-tube with the same area as the AD is given by Eq. (27) (Hansen, 2008):

$$P_{flow} = 0.5\rho\pi R^2 V_\infty^3. \quad (27)$$

With P_{flow} and P, C_p can be calculated, as in Eq. (28) (Hansen, 2008), which is the same as Eq. (1):

$$C_p = P/P_{flow}. \quad (28)$$

The combination of Eq. (26), Eq. (27), and Eq. (28) leads to another relation for calculating C_p, as given by Eq. (29) (Hansen, 2008):

$$C_p = 4a(1-a)^2. \quad (29)$$

METHODOLOGY

Code Structure

Figure 3 shows a diagram of the modified BEM code.

After optimizing the rotor radius and the twist and chord distributions along the blade, the modified BEM algorithm was set up to run the simulations of the HAWTs. After reading the geometry, environment, HAWT project and simulation inputs parameters, the first process of the modified BEM code is the increment of TSR or free stream velocity (depending on the type of simulation). Under that process, there is the incremental subprocess that analyzes each blade element. Under the blade element analysis, there is the iterative subprocess of convergence of the a and b.

Important simulation parameters are the initial guesses, convergence criteria for the a and b and maximum number of convergence attempts. Usually, the initial guess for a is 0 or 0.33, which is the value that maximizes the power coefficient, and the initial guess for the b is 0. However, those values are calibrated, to ensure realistic results. The convergence criteria are the maximum differences between the previous and new calculated induction factors, to consider that the process has converged. The maximum number of attempts of convergence of induction factors is also calibrated, to optimize the results and the processing time.

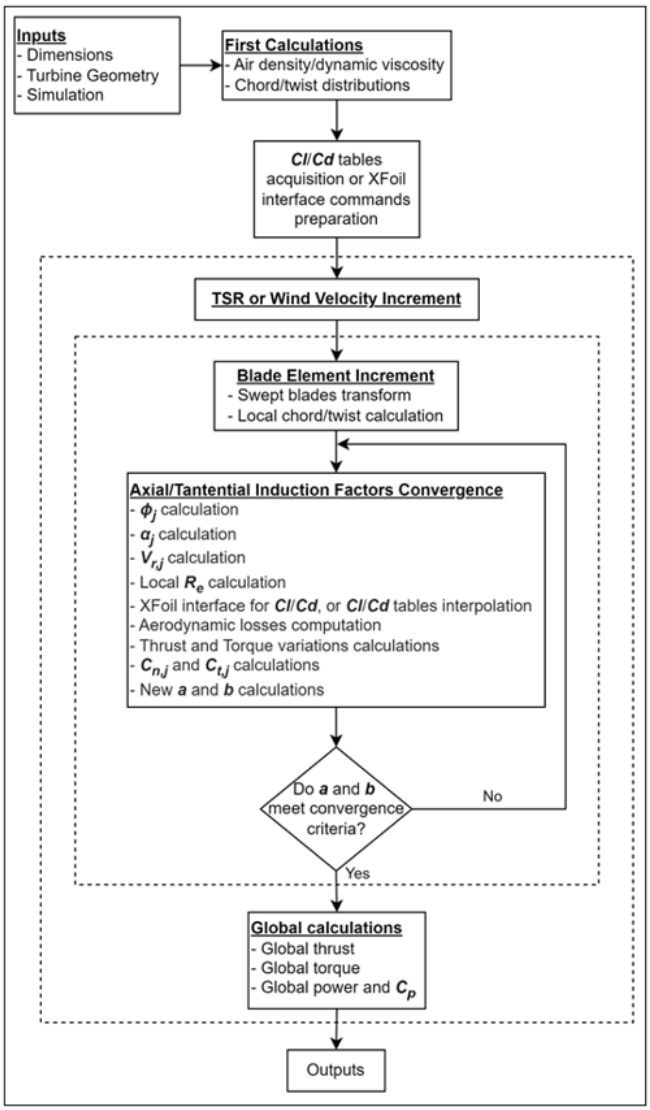

Figure 3. Modified BEM computational processes (Source: Authors' own elaboration)

Lift and Drag Coefficients Sources

The lift and drag coefficients of the airfoil section, C_l and C_d, are inputs of the code and are functions of the angle of attack and Reynolds number. The values of C_l and C_d for each angle of attack can be organized in tables. One table corresponds to a specific Reynolds number. Since several Reynolds numbers appear during one simulation, a set of tables is necessary, to cover as many Reynolds numbers as possible. One set of tables corresponds to a single airfoil. This leads to a high volume of data.

An alternative solution to this problem is to use values of C_l and C_d obtained with XFoil. One disadvantage is that XFoil often does not converge its results for high angles of attack.

Table 1. Optimized and applied geometries for each wind turbine

Airfoil	Radius	Twist hub	Twist tip	Chord hub	Chord tip
Optimized, GOE 419	4.20 m	9.74º	1.05º	0.58 m	0.24 m
Optimized, GOE 101	4.18 m	6.74º	-1.95º	0.44 m	0.18 m
Optimized, GOE 116	4.34 m	7.74º	-0.95º	0.54 m	0.22 m
Optimized, GOE 479	4.26 m	4.99º	-3.70º	0.40 m	0.17 m
Optimized, GOE 526	4.41 m	4.49º	-4.20º	0.43 m	0.18 m
Optimized, GOE 413	4.10 m	4.74º	-3.95º	0.32 m	0.13 m
Optimized, GOE 429	4.49 m	8.74º	0.05º	0.79 m	0.33 m
Optimized, GOE 416A	4.27 m	7.74º	-0.95º	0.57 m	0.23 m
Optimized, GOE 693	4.25 m	5.74º	-2.95º	0.41 m	0.17 m
Optimized, GOE 480	3.91 m	9.74º	1.05º	0.42 m	0.17 m
Optimized, GOE 446	3.90 m	12.00º	3.00º	0.43 m	0.17 m
Optimized, GOE 447	3.89 m	10.74º	2.05º	0.36 m	0.15 m
Optimized, NACA 4412	4.34 m	8.74º	0.05º	0.44 m	0.18 m
Applied (all airfoils)	4.50 m	10.00º	0.00º	0.40 m	0.20 m

However, in a HAWT simulation, those angles are usually small. In order to use computational values of C_l and C_d, an interface between the modified BEM code and XFoil was created. Despite the increase of simulation times, with the interface between the code and XFoil, C_l and C_d are not required as input data from the user.

Optimization and Straight-Bladed HAWTs Base Geometry and Dimensions

Twelve 3-bladed 10-kW HAWTs were designed, with different Göttingen airfoils and the same dimensions, for comparison. Including the HAWT with NACA 4412 airfoil, each wind turbine geometry was optimized for 10 kW power, with linear twist and chord distributions, and a set of dimensions was chosen for all, in order to be simulated with the modified BEM algorithm. The airfoil profiles are: GOE 419, GOE 101, GOE 116, GOE 479, GOE 526, GOE 413, GOE 429, GOE 416A, GOE 693, GOE 480, GOE 446 and GOE 447.

Table 1 shows the optimized dimensions for those airfoils, as well as for NACA 4412. The optimizations were made based on the available C_l and C_d tables. In the case of Göttingen airfoils, those tables were created with XFoil data.

The twist and chord distributions of **Table 1** were linearized at 80% of the radius distance from the hub. For all cases with Göttingen and NACA 4412 airfoils, the code was set to run a maximum of 100 convergence attempts for the a and b, with a convergence criterion of 0.01, and initial guesses of 0.33 for a, and 0 for the b. Instead of providing air density and dynamic viscosity, ambient temperature of 25 °C, relative humidity of 50% and ambient pressure of 100 kPa were provided, for calculating air density and dynamic viscosity.

The B elements was set to 50, and the hub radius was 10% of the rotor radius. The rotor radius was chosen as 4.50 m, based on the optimization results. The code was also set to compute Prandtl losses at the hub and tip of the blades (Eq. [16], Eq. [17], and Eq. [18]), along the radius.

Despite the option of incrementing the wind velocity value, simulations were carried out by incrementing the value of TSR, from 3 to 8, with a step value of 0.20. In order to analyze parameters that change with other variables, a fixed TSR of 6 was chosen. One example is the curve of thrust with the distance from the hub or local radius (radius of the blade element), which needs a constant value of TSR. The fixed wind velocity value (free stream velocity) was 9 m/s.

Table 2. Maximum thickness and camber to chord ratios, and the percentage of the chord in which they are located, for Göttingen airfoils (Airfoil Tools, 2024)

Airfoil	Maximum thickness to chord ratio (t/c)	Maximum chamber to chord ratio (z/c)
GOE 419	5.3% at 30.0% chord	4.1% at 40.0% chord
GOE 101	6.9% at 30.0% chord	4.0% at 30.0% chord
GOE 116	9.3% at 39.8% chord	4.1% at 39.8% chord
GOE 479	11.6% at 30.0% chord	4.0% at 40.0% chord
GOE 526	12.3% at 29.7% chord	4.1% at 39.7% chord
GOE 413	16.4% at 30.0% chord	4.6% at 40.0% chord
GOE 429	11.4% at 30.0% chord	0.2% at 10.0% chord
GOE 416A	11.7% at 29.5% chord	1.3% at 59.6% chord
GOE 693	12.0% at 30.0% chord	3.6% at 40.0% chord
GOE 480	11.8% at 30.0% chord	5.5% at 40.0% chord
GOE 446	12.9% at 29.7% chord	6.3% at 39.7% chord
GOE 447	12.7% at 29.7% chord	8.0% at 39.7% chord

Note. GOE 419, GOE 101, GOE 116, GOE 479, GOE 526, and GOE 413 airfoils have different maximum thickness to chord ratios, with approximately the same maximum chamber to chord ratios, GOE 429, GOE 416A, GOE 693, GOE 480, GOE 446, and GOE 447 have different maximum chamber to chord ratios, with approximately the same maximum thickness as chord ratios, & GOEs were chosen due to their traditional application in wind energy

Since there is not enough information about C_l and C_d values for Göttingen airfoils, the source of those coefficients was XFoil. Despite the convergence issue for high angles of attack, which may exist locally on a HAWT (Hansen, 2008), the angles of attack were monitored during the simulations, and curves of angle of attack with local radius were generated to assure that they are in the range of convergence of XFoil. In the simulations with Göttingen and NACA 4412 airfoils, the C_p accounted for the electromechanics efficiency of the HAWTs. Hence, the C_p was equal to the electromechanics efficiency times the aerodynamic efficiency, which gives the HAWT global efficiency. Electromechanics efficiency was set to 90%. These parameters were applied to all simulations, except the validation's studies, for which simulation parameters are described separately.

Airfoil Maximum Thickness to Chord and Chamber to Chord Ratios

Table 2 shows the maximum thickness to chord ratios (t/c), maximum camber to chord ratios (z/c) and the percentages of the chord in which they are located, for the Göttingen airfoils. In **Table 2**, the airfoils GOE 419, GOE 101, GOE 116, GOE 479, GOE 526, and GOE 413 have different maximum thickness to chord ratios, and approximately the same maximum camber to chord ratios. The airfoils GOE 429, GOE 416A, GOE 693, GOE 480, GOE 446, and GOE 447 have different maximum chamber to chord ratios, and approximately the same maximum thickness to chord ratios. The influences of airfoil maximum thickness to chord and camber to chord ratios over the curves of power with TSR and thrust with radius were evaluated. **Figure 4** shows the curves of maximum thickness to chord ratios (part a), and maximum camber to chord ratios (part b) of **Table 2**, for different Göttingen airfoils (AirfoilTools, 2024).

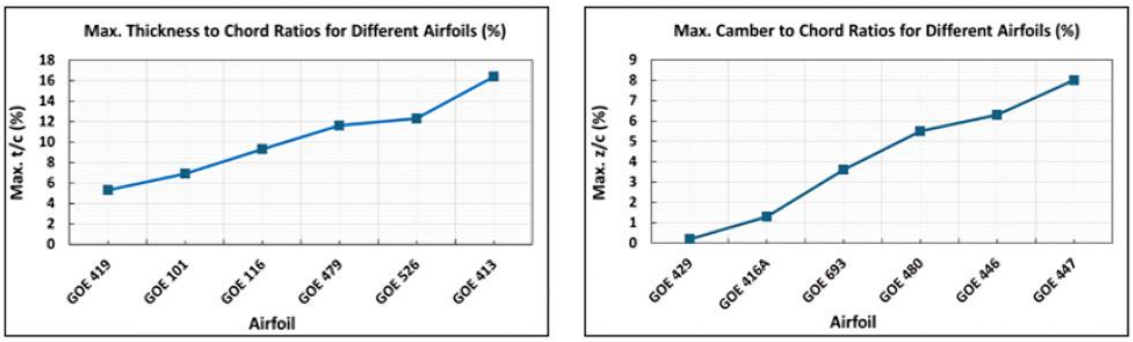

(a) (b)

Figure 4. GOEs geometries (AirfoilTools, 2024): (a) Maximum thickness to chord ratios & (b) Maximum camber to chord ratios (Source: Authors' own elaboration)

HAWTs With Different Tip Sweep Angles

In the study of the influence of the tip sweep angle over the power with TSR, torque with local radius and thrust with local radius curves, for the HAWTs with Göttingen airfoils, the start sweep angle (at the blade root) was kept at 0°, the start sweep point was the blade root, and the tip sweep angles were -40°, 0°, and 40°. The tip sweep angle of 0° is equivalent to a straight blade. Negative tip sweep angles mean that the blade is forward swept, and positive tip sweep angles mean that the blade is backward swept.

VALIDATION

As two ways of running an analysis were implemented, one with providing C_l and C_d as input data, and the other using XFoil to obtain C_l and C_d, a comparative study can be done with results. For the NACA 4412, that is a popular airfoil (Gowda, 2019), there are more sources of experimental C_l and C_d values, as well as JavaFoil (Hepperle, 2018), which is a software that can estimate those coefficients for National Advisory Committee for Aeronautics (NACA) airfoils. Hence, a set of C_l and C_d tables was created. Simulations for a straight-bladed HAWT with NACA 4412 airfoil were run, and results were compared. The rotor geometry and other parameters are the same as the HAWTs with Göttingen airfoils, and they are described together (**Table 1**). The C_p curves with TSR are shown in **Figure 5**.

Both curves have small differences in terms of low TSR values. Disregarding the initial TSR values, for which the first attempts of convergence of induction factors were made, the highest absolute difference is at $TSR = 8$, in which $C_p = 0.42$ for XFoil, and $C_p = 0.47$ for tables, which corresponds to a maximum difference of 10.64%. The results of **Figure 5** show that it is possible to work with both sources of C_l and C_d (tables and XFoil), as long as a reasonable number of tables for different Reynolds numbers are used, with C_l and C_d for a sufficient range of angles of attack. However, it is recommended to compare results generated with the same type of source of C_l and C_d.

The first validation study was made through the comparison of results obtained with the present modified BEM code, and experimental results found in literature (Liu & Janajreh, 2012). The purpose of this validation was to assess the results of the regular BEM code for a straight-bladed HAWT, since it is the base for the swept-bladed HAWT code. The code was set to divide the blades into 50 elements, run a maximum of 100 convergence attempts for the induction factors, with a convergence criterion (absolute differences between current and last values) of 0.001 and initial guesses of 0 for both induction factors. Tables of C_l and C_d were used as input data. It was applied to the NREL S809 airfoil, developed by the national renewable energy laboratory (NREL) (Somers, 1997). The geometry of the wind turbine was reproduced as faithfully as possible, according to the description found in the literature, which is given with other parameters in **Table 3** (Liu & Janajreh, 2012). The results of the first validation are shown in **Figure 6**.

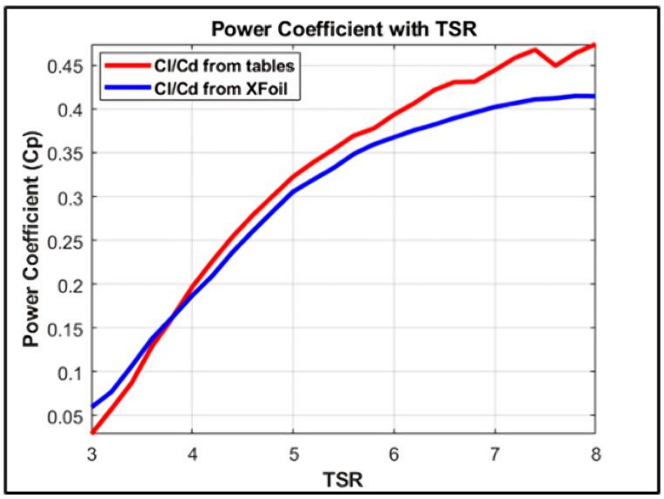

Figure 5. C_p with TSR curves, for different sources of C_l and C_d (NACA 4412 airfoil) (Source: Authors' own elaboration)

Between free stream velocities of 6 and 10 m/s, the results from the present BEM code were close to experimental results. Outside those limits, the errors increase. One reason is that it is not possible to reproduce the exact geometry of a real wind turbine in the BEM code, which assumes simplifying hypotheses for geometry. Hence, the geometries of experimental and simulated HAWTs are not completely the same. Another possible reason for errors is the limited set of C_l and C_d values applied in the simulation. The maximum absolute variation is at $V_\infty = 10\ m/s$, in which $C_p = 0.23$ for

Table 3. Parameters of environment, project and geometry of the first validation simulated HAWT

Parameter	Value
Air density	1.225 kg/m³
Air dynamic viscosity	0.000018205 Pa.s
Airfoil	S809 (AirfoilTools, 2024)
Number of blades	2
Rotor radius	5.70 m
Hub	2% of the rotor radius
Angular velocity	7.54 rad/s
Linear blade twist distribution	Hub: 20.00° & Tip: -2.50°
Linear blade chord distribution	Hub: 0.74 m & Tip: 0.31 m

Table 4. Parameters of environment, project and geometry of the second validation simulated HAWT

Parameter	Value
Air density	1.225 kg/m³
Air dynamic viscosity	0.000018205 Pa.s
Airfoil	FFA-W3-211
Number of blades	3
Rotor radius	20.50 m
Hub	22% of the rotor radius
Angular velocity	2.84 rad/s
Linear blade twist distribution	Hub: 5.00° & Tip: 0.00°
Linear blade chord distribution	Hub: 1.63 m & Tip: 0.27 m

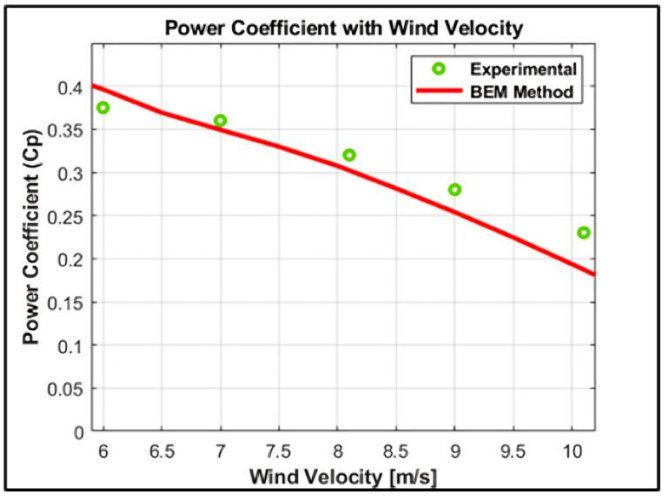

Figure 6. C_p with wind velocity, from experimental results (Liu & Janajreh, 2012) and from the present BEM code (Source: Authors' own elaboration)

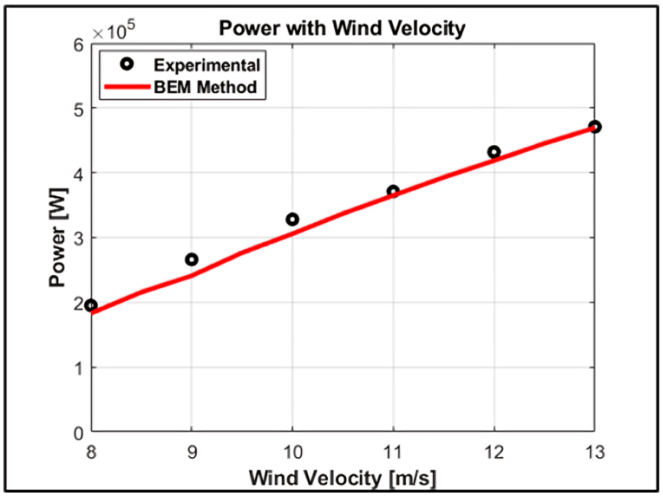

Figure 7. Power with wind velocity, from experimental results (Bak et al., 1999) and from the present BEM code (Source: Authors' own elaboration)

the experimental curve, and $C_p = 0.19$ for the BEM method, corresponding to a difference of 17.39%. In this case, the initial values of simulated wind velocities were excluded from the curve, which allowed the use of first shown values in the error measurement.

A second validation study was made through the comparison of results of a different straight-bladed HAWT, with results found in literature (Kulunk & Yilmaz, 2009). As the first validation, the code was set to divide the blades into 50 elements, run a maximum of 100 convergence attempts for the induction factors, with a convergence criterion of 0.01, and initial guesses of 0.33 for a, and 0 for the b. Tables of C_l and C_d were used as input data. The geometry of the wind turbine was reproduced as faithfully as possible, according to the description found in the literature, which is given with other parameters in **Table 4** (Bak et al., 1999).

The results of the second validation are shown in **Figure 7**. The maximum absolute difference of experimental results and the results of this work occurred for $V_\infty = 9\ m/s$. At this point, the experimental study reported a power of 266 kW (Bak et al., 1999), and the power obtained through BEM code was 241 kW, which corresponds to a difference of 9.40%. Once again, one of the reasons for the errors is the differences between the geometry of experimental HAWT and the geometry of simulated HAWT, with the simplifying hypotheses of BEM method. As in the first validation, another reason for the errors is the limited set of C_l and C_d values used.

The differences in experimental and simulated results for both validations were expected due to the simplifying hypotheses for the HAWTs geometries and the limitations in input data. The hub shapes and the blade root connections with the hub were not considered. Also, the twist and chord distributions were linearized. In future work, the geometry level of detail can be improved, as well as more tables of C_l and C_d tables can be applied to reduce errors. Considering that those differences are small and have reasonable explanations, the modified BEM code used in this work was validated.

RESULTS AND DISCUSSION

Airfoil Maximum Thickness to Chord Ratios

Airfoil maximum thickness to chord ratios results were evaluated through the curves of power with TSR and thrust in blade element with local radius. The start sweep angle was kept at 0°, from the blade root. The evaluated tip sweep angles were -40°, 0°, and 40°.

Figure 8, **Figure 9**, and **Figure 10** show the curves of power with TSR and thrust in blade element with local radius for $TSR = 6$, for HAWTs with airfoils with different maximum thickness to chord ratios and similar maximum camber to chord ratios, with tip sweep angles equal to -40°, 0°, and 40°, respectively. In **Figure 8**, **Figure 9**, and **Figure 10**, some curves have sudden changes, as the power with TSR curves of

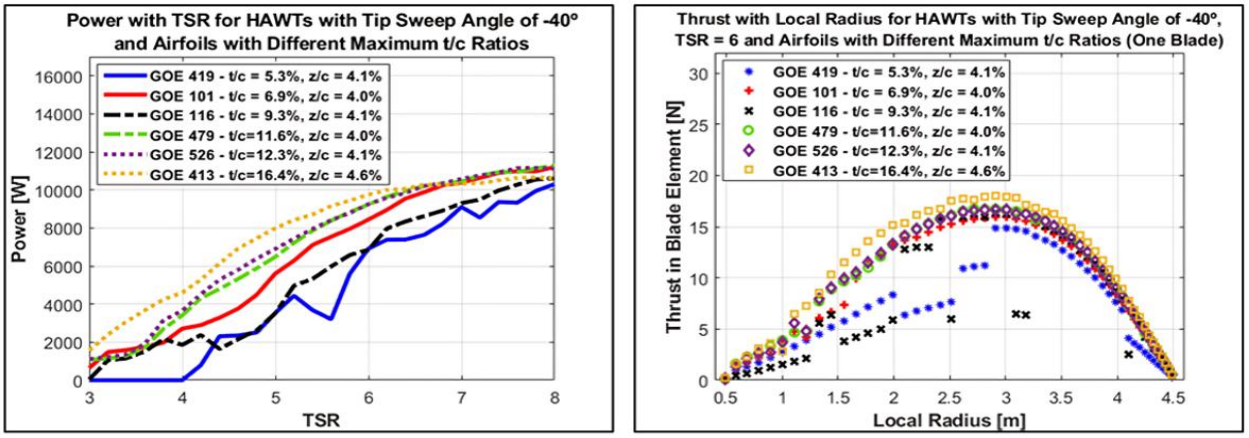

(a) (b)

Figure 8. Results for HAWTs with airfoils with different maximum thickness to chord ratios, for tip sweep angle equal to -40°: (a) Power with TSR & (b) Thrust in blade element with local radius for a single blade and $TSR = 6$ (Source: Authors' own elaboration)

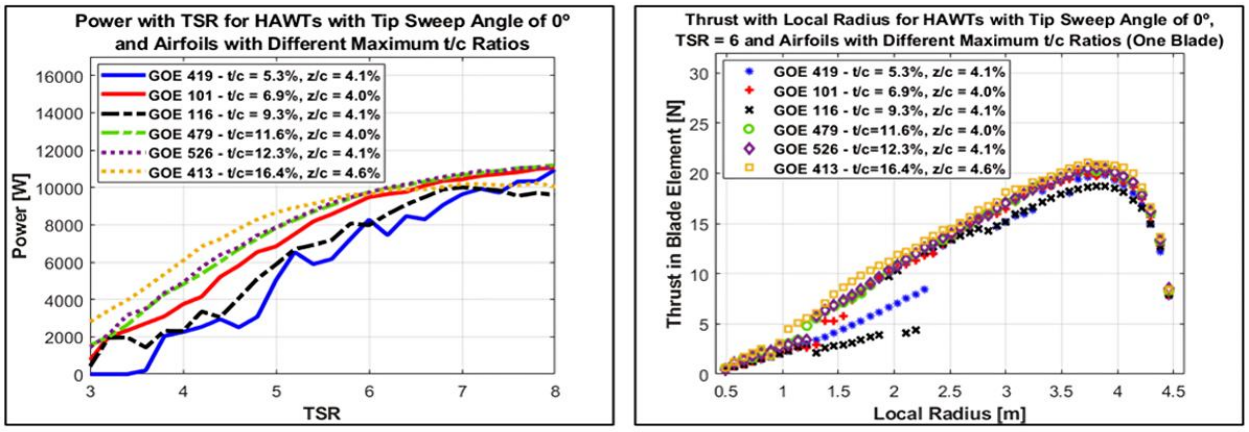

(a) (b)

Figure 9. Results for HAWTs with airfoils with different maximum thickness to chord ratios, for tip sweep angle equal to 0°: (a) Power with TSR & (b) Thrust in blade element with local radius for a single blade and $TSR = 6$ (Source: Authors' own elaboration)

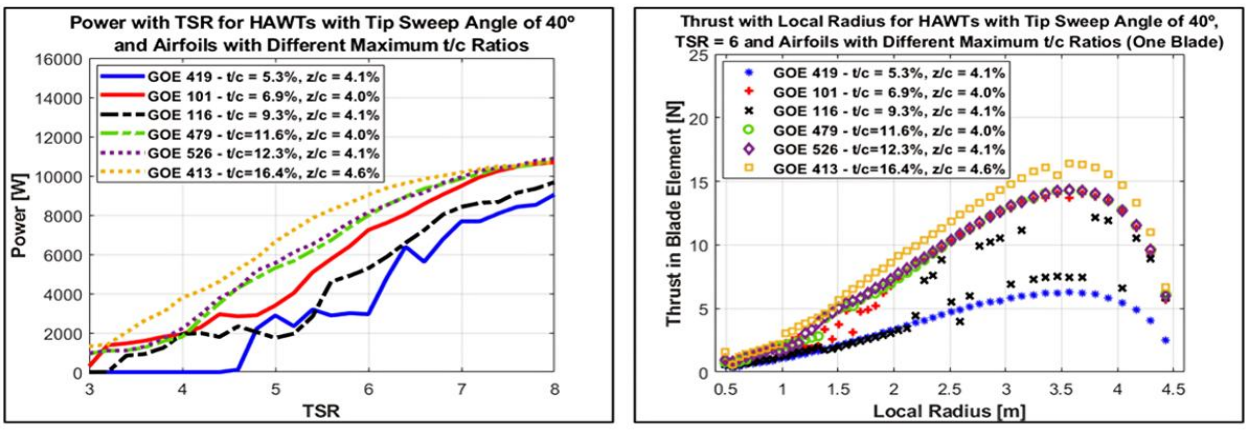

(a) (b)

Figure 10. Results for HAWTs with airfoils with different maximum thickness to chord ratios, for tip sweep angle equal to 40°: (a) Power with TSR & (b) Thrust in blade element with local radius for a single blade and $TSR = 6$ (Source: Authors' own elaboration)

GOE 419 airfoil. The sudden changes occur due to points of non-convergence, originated in XFoil simulations. However, this did not affect the analyses and comparisons.

HAWTs with GOE 413 airfoil ($t/c = 16.4\%$) presented the highest power generation for TSR under 6, for all tip sweep angles (-40°, 0°, and 40°). This leads to the conclusion that

airfoils with high maximum thickness to chord ratios produce more power, for lower TSR values.

On the other hand, for TSR equal or greater than 7, GOE 101 ($t/c = 6.9\%$), GOE 479 ($t/c = 11.8\%$), and GOE 526 ($t/c = 12.3\%$) airfoils seem to produce more power for all tip sweep angles, due to a more pronounced growth of their power with TSR curves. This leads to the conclusion that airfoils with low and moderate maximum thickness to chord ratios produce more power at higher TSR values.

However, results showed a lower limit for maximum thickness to chord ratios for power increase, since GOE 419 airfoil ($t/c = 5.3\%$), which has the lowest maximum thickness to chord ratio, did not show the highest power generation for high TSR values.

The curves of part a in **Figure 9** for GOE 116 and GOE 413, airfoils show a small drop in power generation for high TSR values. The curves of part a in **Figure 8** and **Figure 10** for the same airfoils suggest that swept-bladed HAWTs avoid the power generation drop observed in straight-bladed HAWTs, which is one benefit of blades sweep.

Part b in **Figure 8**, **Figure 9**, and **Figure 10** suggest that the increase in power generation caused by airfoils with high maximum thickness to chord ratios has a negative effect, which is the increase of the thrust along the blade. HAWTs with GOE 413 and GOE 526 airfoils, which have the highest maximum thickness to chord ratios, presented the highest power generations for low TSR values. They also produced the highest thrust values of all blades, for tip sweep angles of -40°, 0°, and 40°. On the other hand, HAWTs with GOE 419 airfoil, which has the lowest maximum thickness to chord ratio, presented the lowest power generation for low TSR values. They also produced one of the lowest thrust values along the blade, for all tip sweep angles (-40°, 0°, and 40°).

High thrust values along the blade suggest the presence of high mechanical loads over the blade and tower structure. If, on the one hand, HAWTs with GOE 413 and GOE 526 airfoils achieved the highest thrust results, on the other hand, the greater thickness of these airfoils produces more resistant blades. Hence, for TSR less or equal to 6, HAWTs with GOE 413 airfoil seem to present the best results, due to the highest power generation, despite the high thrust results.

Table 5. Best performing airfoils in terms of power generation, for different maximum thickness to chord ratios

Airfoil	Maximum thickness to chord ratio (t/c)
GOE 413	16.4% at 30.0% chord
GOE 526	12.3% at 29.7% chord
GOE 479	11.6% at 30.0% chord

Table 5 shows the ranking of the best performing airfoils in terms of power generation, for different maximum thickness to chord ratios.

Figure 11 shows the flow angle (part a) and the angle of attack (part b) curves with the local radius, for HAWTs with GOE 413 airfoil, TSR equal to 6 and different tip sweep angles. Part b in **Figure 11** shows that the angles of attack are in the range of XFoil convergence.

According to Roy et al. (2021), airfoils with higher thickness ratios produce maximum lift to drag ratios, for angles of attack higher than 8°, which corresponds to the most part of the curves of part b in **Figure 11**. This explains the higher power generation and thrust results for airfoils with high maximum thickness to chord ratios, such as GOE 413, GOE 526, and GOE 479.

Airfoil Maximum Chamber to Chord Ratios

As in the airfoils maximum thickness to chord ratios cases, airfoils maximum camber to chord ratios were evaluated through the curves of power with TSR and thrust in blade element with local radius. The start sweep angle was kept at 0°, from the blade root. The evaluated tip sweep angles were -40°, 0°, and 40°. **Figure 12**, **Figure 13**, and **Figure 14** show the curves of power with TSR and thrust in blade element with local radius for $TSR = 6$, for HAWTs with airfoils with different maximum camber to chord ratios and similar maximum thickness to chord ratios, with tip sweep angles equal to -40°, 0°, and 40°, respectively.

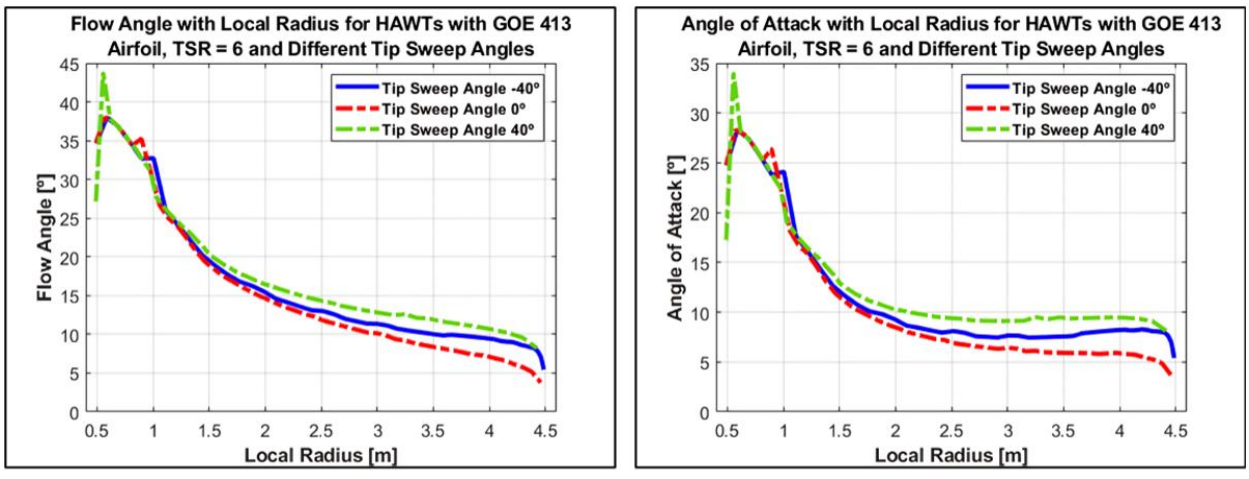

(a) (b)

Figure 11. Flow angle (a) and angle of attack (b) with local radius for HAWTs with GOE 413 airfoil, $TSR = 6$ and different tip sweep angles (-40°, 0°, and 40°) (Source: Authors' own elaboration)

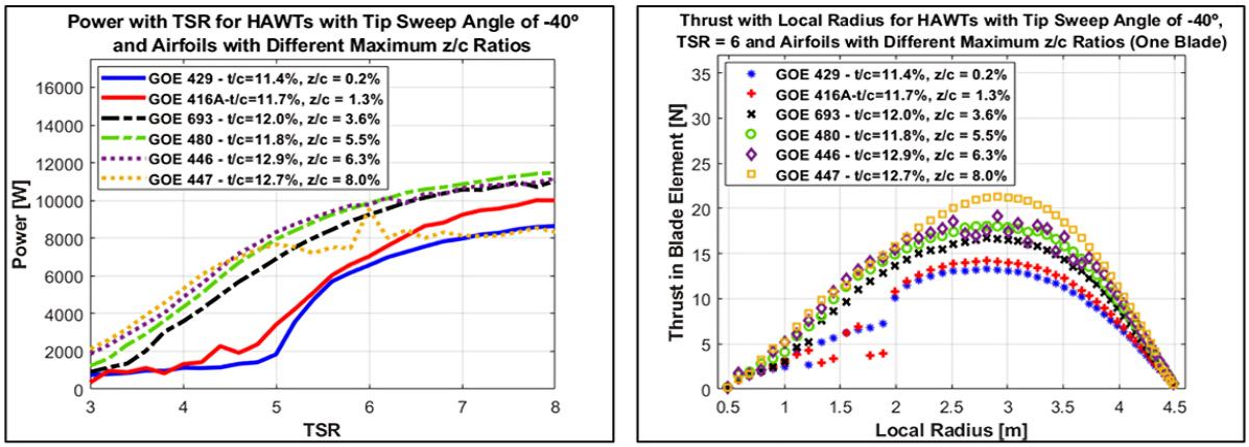

(a) (b)

Figure 12. Results for HAWTs with airfoils with different maximum camber to chord ratios, for tip sweep angle equal to -40°: (a) Power with TSR & (b) Thrust in blade element with local radius for a single blade and $TSR = 6$ (Source: Authors' own elaboration)

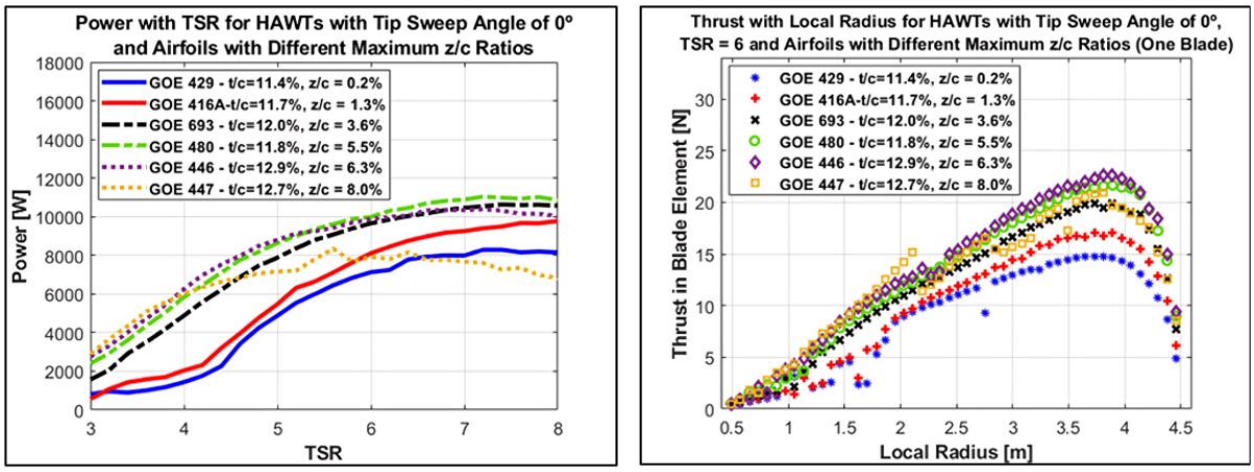

(a) (b)

Figure 13. Results for HAWTs with airfoils with different maximum camber to chord ratios, for tip sweep angle equal to 0°: (a) Power with TSR & (b) Thrust in blade element with local radius for a single blade and $TSR = 6$ (Source: Authors' own elaboration)

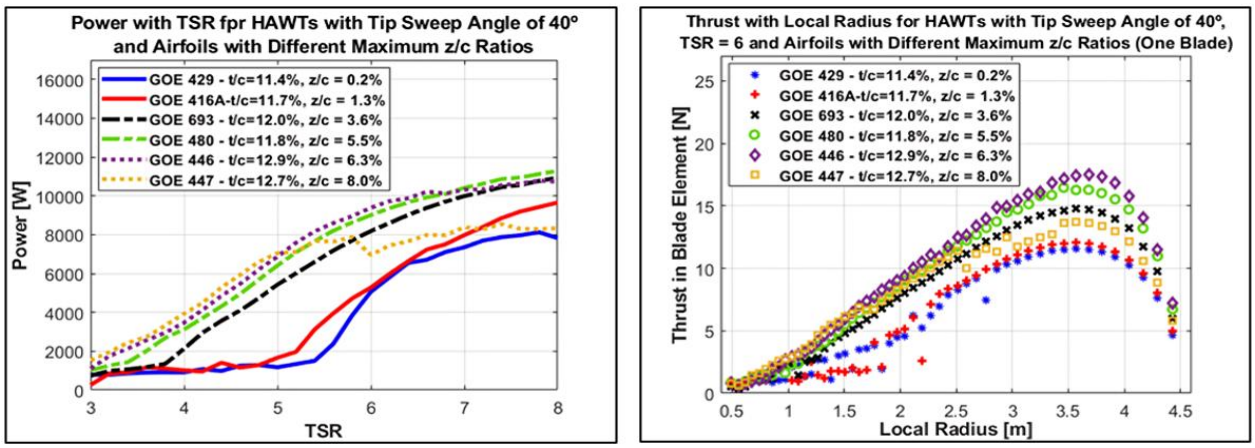

(a) (b)

Figure 14. Results for HAWTs with airfoils with different maximum camber to chord ratios, for tip sweep angle equal to 40°: (a) Power with TSR & (b) Thrust in blade element with local radius for a single blade and $TSR = 6$ (Source: Authors' own elaboration)

In part a in **Figure 12**, **Figure 13**, and **Figure 14**, it is possible to observe that HAWTs with GOE 447 airfoil ($z/c = 8.0\%$), which has the highest maximum camber to chord ratio, produce the highest power for TSR under 4, for all blade tip sweep angles (-40°, 0°, and 40°). For TSR over 4, HAWTs with airfoils with intermediate maximum chamber to chord ratios

produced more power, as was the case of GOE 693 ($z/c = 3.6\%$), GOE 480 ($z/c = 5.5\%$), and GOE 446 ($z/c = 6.3\%$) airfoils. Airfoils with low maximum camber to chord ratios, such as GOE 429 ($z/c = 0.2\%$) presented the lowest power generation for TSR under 6, for all tip sweep angles. These results lead to the conclusion that airfoils with moderate maximum camber to chord ratios produce more power for all TSR values. Using GOE 446 airfoil as an example, the comparison of its performance in part a in **Figure 12**, **Figure 13**, and **Figure 14** suggest that swept-bladed HAWTs avoid the power generation drop observed in straight-bladed HAWTs, for airfoils with intermediate and high maximum chamber to chord ratios at TSR over 6, which is one benefit.

As a general result, for swept-bladed HAWTs, airfoils with intermediate maximum camber to chord ratios, such as GOE 693, GOE 480, and GOE 446, show most consistent power generation results, for TSR between 3 and 8. The GOE 480 airfoil has a similar maximum camber to chord ratio as GOE 413 airfoil, which was considered the best airfoil in the maximum thickness to chord analysis.

Once again, airfoils that showed the highest power generations also showed the highest thrust along the blade, as was the case of GOE 480 and GOE 446 (part b in **Figure 12**, part b in **igure 13**, and **Figure 14**,). In other words, the increase in power generation has a negative effect, which is the thrust rise, as it was observed in the airfoil maximum thickness to chord analysis.

Table 6 shows the ranking of the best performing airfoils in terms of power generation, for different maximum chamber to chord ratios.

According to Roy et al. (2021), airfoils with higher camber ratios increase lift and drag coefficients, as well as the lift to drag ratio. This explains the higher power generation and thrust results for airfoils with high and moderate maximum camber to chord ratios, such as GOE 446, GOE 480, and GOE 693.

In the study of Veloso et al. (2023), circular arc airfoils were applied to swept-bladed HAWTs. Those are airfoils with high cambers. According to their results, the thrust of swept blades with circular arc airfoils is not always less than the thrust of straight blades with the same airfoils, which seems to be due to the complex behavior of the boundary layer detachment on the airfoil at low Reynolds numbers. This can explain the low power generation and average to high thrust of the airfoil GOE 447, which has the highest maximum camber to chord ratio between the airfoils applied on this study.

Table 6. Best performing airfoils in terms of power generation, for different maximum chamber to chord ratios

Airfoil	Maximum chamber to chord ratio (t/c)
GOE 446	6.3% at 39.7% chord
GOE 480	5.5% at 40.0% chord
GOE 693	3.6% at 40.0% chord

Tip Sweep Angle for HAWTs With GOE 413 Airfoil

In the analysis of the influence of airfoil maximum thickness to chord ratio over the power generation with TSR and thrust with local radius curves, GOE 413 airfoil presented the best results. In the analysis of the influence of airfoil maximum camber to chord ratio over the power generation with TSR and thrust with local radius curves, GOE 480 and GOE 446 airfoils presented the best results for power generation. Since GOE 413 and GOE 480 have similar maximum camber to chord ratios ($z/c = 4.6\%$ and $z/c = 5.5\%$, respectively), GOE 413 airfoil was selected for the study of the influence of the tip sweep angle over power and C_p with TSR curves, and torque and thrust with local radius curves.

Figure 15 shows the curves of power (part a) and C_p (part b) with TSR, for HAWTs with GOE 413 airfoil, with tip sweep angles of -40°, 0°, and 40°.

As it was observed before, the curves of **Figure 15** suggest that swept-bladed HAWTs avoid the C_p and power drop at high TSR values, in this case, for TSR values above 6. The straight-bladed HAWT (tip sweep angle of 0°) showed the highest power generation for TSR between 3 and 6. For TSR between 6 and 8, the swept-bladed HAWT with tip sweep angle of -40° showed the highest power generation. For TSR above 7, the swept-bladed HAWT with tip sweep angle of 40° produce

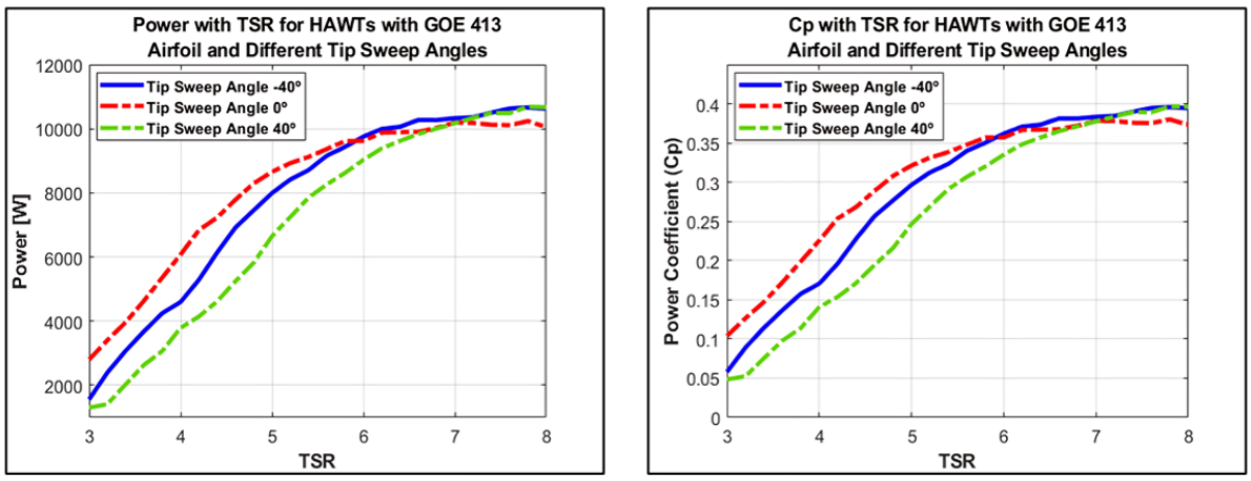

(a) (b)

Figure 15. Power (a) and C_p (b) with TSR, for HAWTs with GOE 413 airfoil and different tip sweep angles (-40°, 0°, and 40°) (Source: Authors' own elaboration)

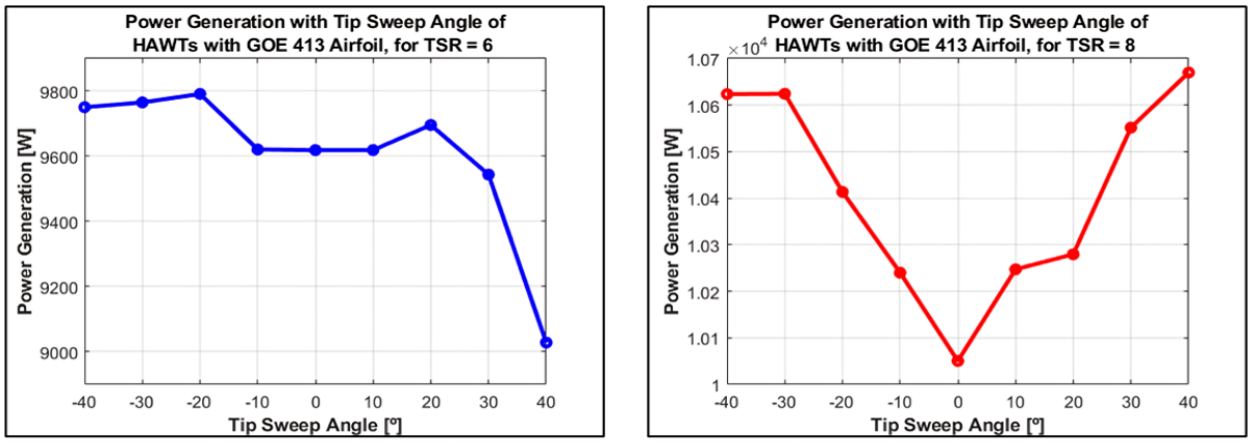

(a) (b)

Figure 16. Power generation with tip sweep angle, for HAWTs with GOE 413 airfoil: (a) $TSR = 6$ & (b) $TSR = 8$ (Source: Authors' own elaboration)

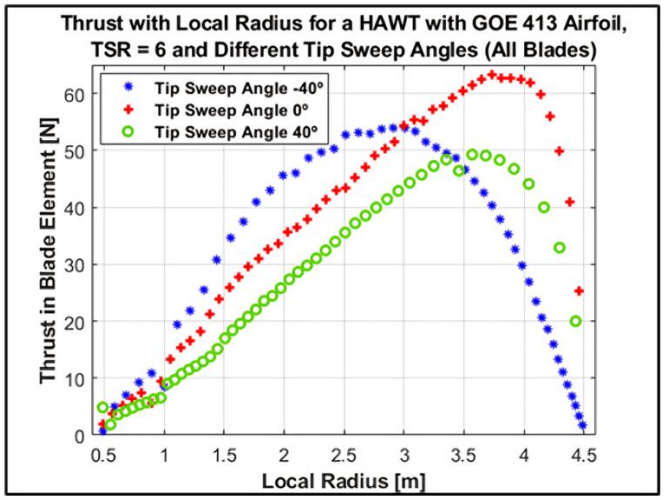

Figure 17. Thrust with local radius for HAWTs with GOE 413 airfoil, $TSR = 6$ and different tip sweep angles (Source: Authors' own elaboration)

more power than the straight-bladed HAWT. As a general result, the swept-bladed HAWT with -40° tip sweep angle presented the most consistent power generation results with TSR variation.

Figure 16 shows the power generation with tip sweep angle between -40° and 40°, for HAWTs with GOE 413 airfoil, at TSR of 6 (part a) and 8 (part b).

In part a in **Figure 16**, for HAWTs with GOE 413 airfoil and $TSR = 6$, the increase of the tip sweep angle above 20° reduced the power generation. At -20° tip sweep angle, the power generation was the highest, which may indicate a limit for the growth of power generation with the reduction of negative tip sweep angles. The power generation of -20° blade tip sweep angle was 9791.41 W, 1.79% higher than the power generation of 0° blade tip sweep angle (9619.01 W).

In part b in **Figure 16**, for $TSR = 8$, the power generation drops to a local minimum for tip sweep angle of 0° (10,050.24 W) and increases with the increase of positive tip sweep angles and the reduction of negative tip sweep angles. These results can also be seen in part b in **Figure 16**. The maximum power generation of negative tip sweep angles was 10,624.30 W, for -30° tip sweep angle, which is 5.71% higher than the power generation of 0° blade tip sweep angle. For positive tip sweep angles, the maximum power generation was 10,669.81 W, for 40° tip sweep angles, which is 6.16% higher than the power generation of 0° blade tip sweep angle.

As in previous analyses, the curves of part b in **Figure 16** also suggest that forward and backward blade tip sweep angles avoid the power generation drop for high TSR values, in this case, for TSR equal 8 or higher.

Figure 17 shows the curves of thrust with local radius for HAWTs with GOE 413 airfoil, TSR of 6 and different tip sweep angles. Results suggest that swept-bladed HAWTs produce thrust alleviation over the blade, for $TSR = 6$, which can reduce mechanical loads over the blades and over the wind turbine structure.

Figure 18 shows the curves of total thrust with tip sweep angle between -40° and 40°, for TSR equal to 6 (part a), and TSR equal to 8 (part b).

Part a and part b in **Figure 18** confirm that positive and negative tip sweep angles produce load alleviation over the blades, for TSR equal 6 and 8. For both TSR values, the thrusts reached the maximum values for tip sweep angle equal to 0°. The thrusts of HAWTs with 40° blade tip sweep angle were 32.69% and 31.92% lower than the thrust of HAWTs with 0° blade tip sweep angle, for $TSR = 6$ and $TSR = 8$, respectively.

The thrust is responsible for the distribution of loads along the blades. According to Otero and Ponta (2018), there are fluctuations on these loads, which generates fatigue in the blades structure. In future extremely large wind turbines, these loads could become determinant by limiting lifespan due to fatigue of structural and mechanical components or producing catastrophic failure after triggering resonance or unstable behavior at some particular frequency.

Considering the results of part a in **Figure 16** and **Figure 18**, for HAWTs with GOE 413 airfoil, -20° tip sweep angle reached the best results of power generation and thrust for TSR equal 6 (9,791.41 W and 1,817.51 N, respectively). In part b in **Figure 16** and **Figure 18**, for HAWTs with GOE 413 airfoil, 40° tip sweep angle reached the best results in terms of power

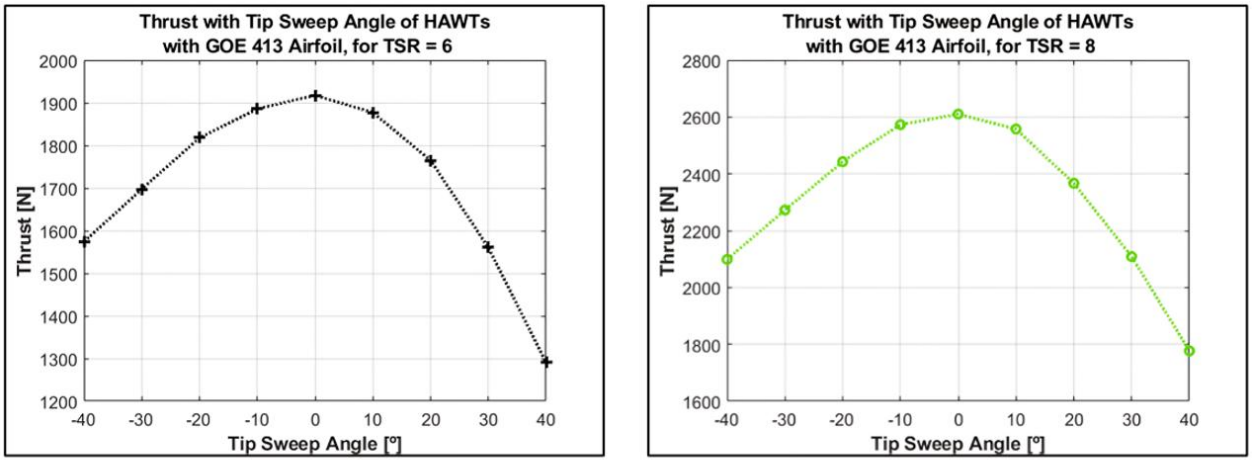

(a) (b)

Figure 18. Total thrust with tip sweep angle, for HAWTs with GOE 413 airfoil: (a) $TSR = 6$ & (b) $TSR = 8$ (Source: Authors' own elaboration)

generation (10,669.81 W) and load alleviation (thrust equal to 1,776.79 N), for TSR equal 8.

Torque and Thrust Variation With Local Radius for HAWTs With GOE 413 Airfoil

The selection of GOE 413 airfoil was kept for the torque with local radius analysis, as well as for further analysis of the thrust with local radius. Here, the goal was to evaluate, for different tip sweep angles, the contribution of different sectors of the blade for the torque generation. Also, the contribution of different sectors of the blade for the thrust generation was evaluated, for different tip sweep angles.

The torque produced in a wind turbine is associated with its power generation, which is the total torque times the angular velocity of the blades. **Figure 19** show the torque in blade element for a single blade with the local radius, for HAWTs with GOE 413 airfoil, $TSR = 6$ and tip sweep angles of -40°, 0°, and 40°. The curves are divided according to different blade zones, measured along the blade length, R_b: from the root to 20% R_b (0.45 m to 1.26 m from the center of the hub), from 20% R_b to 90% R_b (1.26 m to 4.10 m from the center of the hub), and from 90% R_b to the blade tip (4.10 m to 4.50 m from the center of the hub). The contribution of intermediate regions of blades tends to be the highest, since it does not suffer induced aerodynamic losses as in the root and tip of the blades (Canale et al., 2018).

The results of **Figure 19** are summarized in **Table 7**, **Table 8**, and **Table 9**, which show the sums and contributions of each blade sector to total torque and power generation. The sums of torque in blades elements were obtained from the curves of **Figure 19**. The percentage contributions of blades sections were calculated through the torque values. After that, the same

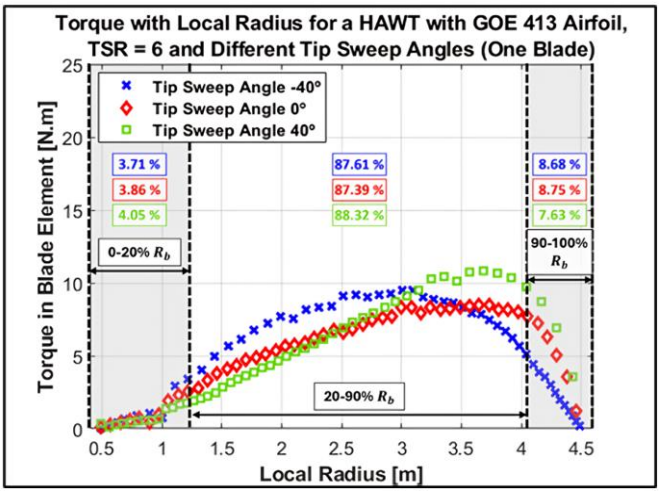

Figure 19. Torque with radius and contributions to torque of different blade zones of HAWTs with GOE 413 airfoil, $TSR = 6$ and different tip sweep angles (single blade) (Source: Authors' own elaboration)

percentages were applied to the total power generation, resulting in the power generation at each blade section.

For $TSR = 6$, the highest power generation was achieved by the HAWT with -40° blade tip sweep angle (9,750.61 W), while the HAWT with 40° tip sweep angle showed the lowest power generation (9,028.35 W). As expected, most of the torque/power generation in swept-bladed and straight-bladed HAWTs occurred in the blade region located between 20% and 90% of R_b. The percentual contribution of the mid-sections of the blades to torque/power generation were the highest for the swept-bladed HAWT with 40° tip sweep angle (88.32%),

Table 7. Sum of torque/power in blades elements, for the HAWT with GOE 413 airfoil, $TSR = 6$ and -40° tip sweep angle

Region of the blade	Sum of torque in blades elements ($N.m$)	Sum of power in blades elements (W)	Contribution to total torque/power
0 to 20% R_b	30.18	361.75	3.71%
20 to 90% R_b	711.85	8,,542.51	87.61%
90 to 100% R_b	70.52	846.35	8.68%
All blades	812.55	9,750.61	100%

Table 8. Sum of torque/power in blades elements, for the HAWT with GOE 413 airfoil, $TSR = 6$ and 0° tip sweep angle

Region of the blade	Sum of torque in blades elements ($N.m$)	Sum of power in blades elements (W)	Contribution to total torque/power
0 to 20% R_b	30.95	371.29	3.86%
20 to 90% R_b	700.51	8406.05	87.39%
90 to 100% R_b	70.13	841.67	8.75%
All blades	801.59	9619.01	100%

Table 9. Sum of torque/power in blades elements, for the HAWT with GOE 413 airfoil, $TSR = 6$ and 40° tip sweep angle

Region of the blade	Sum of torque in blades elements ($N.m$)	Sum of power in blades elements (W)	Contribution to total torque/power
0 to 20% R_b	30.46	365.65	4.05%
20 to 90% R_b	664.52	7,973.84	88.32%
90 to 100% R_b	57.38	688.86	7.63%
All blades	752.36	9,028.35	100%

followed by the HAWT with -40° blade tip sweep angle (87.61%) and by the straight-bladed HAWT (87.39%).

Table 7, **Table 8**, and **Table 9** show that the swept-bladed HAWT with -40° tip sweep angle produced more absolute power and torque at the tip region (846.35 W and 70.52 N.m, 8.68% of total power/torque) together with the straight-bladed HAWT (841.67 W and 70.13 N.m, 8.75% of total power/torque), compared to the swept-bladed HAWT with 40° tip sweep angle (688.86 W and 57.38 N.m, 7.63% of total power/torque). This result suggests the tip region contributes more to the total torque in the case of -40° and 0° tip sweep angles than the 40° tip sweep angle.

Despite small differences, as a general result, the contributions of each section of the blades to the power/torque were similar for the 3 HAWTs analyzed.

Figure 20 shows the thrust distributions along the radius, for HAWTs with GOE 413 airfoil, $TSR = 6$ and tip sweep angles of -40°, 0°, and 40°.

Thrust curves were divided into the same blade sections as torque curves. They also show the sums and contributions of each blade sector to total thrust. **Table 10**, **Table 11**, and **Table 12** show the sums of the thrust in each blade sector, as well as the total thrust over the blades, for HAWTs with GOE 413 airfoil, TSR equal to 6 and tip sweep angles of -40°, 0°, and 40°, respectively.

In **Figure 20**, the curve for 0° tip sweep angle is less smooth than the curves of -40° and 40° tip sweep angles, which indicates that straight-bladed HAWTs may concentrate more loads than swept-bladed HAWTs. This can be seen through the

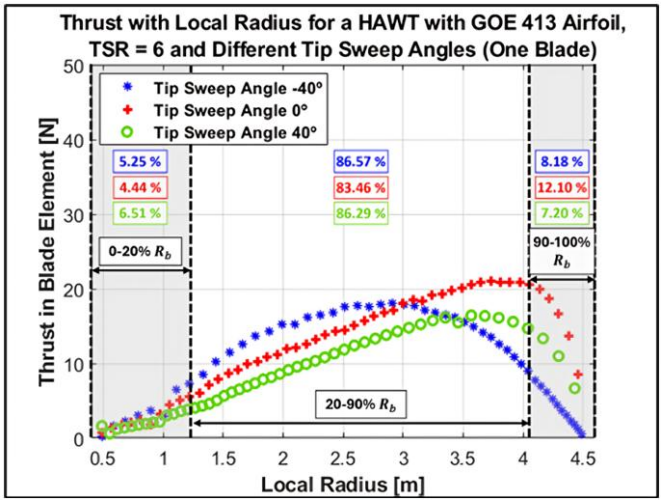

Figure 20. Thrust with radius and contributions to thrust of different blade zones of HAWTs with GOE 413 airfoil, $TSR = 6$ and different tip sweep angles (single blade) (Source: Authors' own elaboration)

thrust peak (21.06 N) around 90% R_b, in the curve of the HAWT with 0° tip sweep angle, that have dropped by more than 22% in swept-bladed HAWTs.

The total thrust of the HAWT with 0° tip sweep angle (1,917.46 N) was the highest among the three HAWTs analyzed, due to the load alleviation effect of blade tip sweep angles different than 0°. The results show the lowest percentual contribution of the tip region for blades with 40°

Table 10. Sum of thrust in blades elements, for the HAWT with GOE 413 airfoil, $TSR = 6$ and -40° tip sweep angle

Region of the blade	Sum of thrust in blades elements (N)	Contribution to total thrust
0 to 20% R_b	82.56	5.25%
20 to 90% R_b	1,362.47	86.57%
90 to 100% R_b	128.81	8.18%
All blades	1,573.84	100%

Table 11. Sum of thrust in blades elements, for the HAWT with GOE 413 airfoil, $TSR = 6$ and 0° tip sweep angle

Region of the blade	Sum of thrust in blades elements (N)	Contribution to total thrust
0 to 20% R_b	85.16	4.44%
20 to 90% R_b	1,600.37	83.46%
90 to 100% R_b	231.93	12.10%
All blades	1,917.46	100%

Table 12. Sum of thrust in blades elements, for the HAWT with GOE 413 airfoil, $TSR = 6$ and 40° tip sweep angle

Region of the blade	Sum of thrust in blades elements (N)	Contribution to total thrust
0 to 20% R_b	84.05	6.51%
20 to 90% R_b	1,113.68	86.29%
90 to 100% R_b	92.87	7.20%
All blades	1,290.60	100%

tip sweep angles in comparison with straight blades and blades with -40° tip sweep angles.

The load alleviation effect over swept blades occurred at the mid-sections and at the tips of the blades, for the HAWTs with -40° and 40° tip sweep angles.

CONCLUSIONS

In this work, a modified BEM code for swept-bladed HAWTs was implemented in MATLAB, in order to simulate different concepts of HAWTs with Göttingen airfoils, with different blade tip sweep angles. The code was validated by comparison of results found in literature.

The airfoil maximum thickness to chord analysis showed that airfoils with high maximum thickness to chord ratios produce more power for all tip sweep angles, at low TSR values (TSR less or equal 6). On the other hand, airfoils with low and moderate maximum thickness to chord ratios produce more power for all tip sweep angles, at high TSR values (TSR above 6).

The high power generation for low TSR values of airfoils with high maximum thickness to chord ratios produces a negative effect, which is the high thrust values along the blades, for HAWTs with -40°, 0°, and 40° tip sweep angles. However, thicker airfoils also result in more resistant blades, which makes airfoils with high maximum thickness to chord ratios a good choice for increasing power generation.

The maximum camber to chord analysis showed that airfoils with moderate maximum camber to chord ratios can produce more power for TSR values above 4. However, they also produce more thrust along the blades. As a general result of the airfoil analysis, swept-bladed HAWTs with GOE 413 airfoil and -40° blade tip sweep angle produced most consistent results, in terms of power generation.

The tip sweep angles analysis showed that positive and negative tip sweep angles avoid the power generation drop at high TSR values. Also, for TSR equal 6 and 8, high positive and negative tip sweep angles produce load alleviation along the blades, which is good for the wind turbine structure. For $TSR = 6$, the maximum power generation was 9,791.41 W, for -20° blade tip sweep angle, which is 1.79% higher than the power generation of 0° blade tip sweep angle (9,619.01 W). The corresponding thrust was 1817.51 N. For $TSR = 8$, the maximum power generation of negative tip sweep angles was 10,624.30 W, for -30° tip sweep angles (5.71% higher than the power of 0° blade tip sweep angle), and the maximum power generation for positive tip sweep angles was 10,669.81 W, for 40° tip sweep angle (6.16% higher than the power of 0° blade tip sweep angle). The corresponding thrusts were 1,817.51 N and 1,776.79 N, for -30° and 40° tip sweep angles, respectively. The thrust of HAWTs with 40° blade tip sweep angle were 32.69% and 31.92% lower than the thrust of HAWTs with 0° blade tip sweep angle, for TSR equal 6 and 8, respectively.

Results from the HAWTs torque and power analyses showed that the higher torque and power generation of HAWTs with -40° tip sweep angle and TSR equal 6 may be due to an increase in the torque/power generation at the mid-sections and at the blades tips. In the study of the thrust along the blades, results showed that the load alleviation effect caused by the -40° and 40° tip sweep angles occurred at the mid-sections and at the tips of the blades.

The results of this work showed that swept-bladed HAWTs have a good potential for increase the power generation, compared to the correspondent straight-bladed HAWTs. Also, the tip sweeping angles may result in load alleviation, which is good for the wind turbine structure.

Author contributions: KARI: conceptualization, project, writing – review & editing; **PAAB:** methodology, writing – original draft. All co-authors have agreed with the results and conclusions.

Funding: This paper received no funding.

Acknowledgements: The authors wish to thank the Fundação para Inovações Tecnológicas (FITec) for the doctoral scholarship to the second author.

Ethical statement: The authors stated that the study does not require approval from an ethics committee since this work did not involve investigation or experiments on animals or humans.

Declaration of interest: No conflict of interest is declared by the authors.

Data sharing statement: Data supporting the findings and conclusions are available upon request from the corresponding author.

REFERENCES

Ahmad, A., Loya, A., Ali, M., Iqbal, A., Baig, F., & Afzal, A. (2020). Roadside vertical axis wind turbine (VAWT): An effective evolutionary design for Australian highway commuters with minimum dynamic stall. *Engineering, 12*, 601-616. https://doi.org/10.4236/eng.2020.129042

AirfoilTools. (2024). Airfoil Profiles. *AirfoilTools*. http://www.airfoiltools.com

Bak, C., Fuglsang, P., Sørensen, N. N., Madsen, H. A., Shen, W. Z., & Sørensen, J. N. (1999). *Airfoil characteristics for wind turbines*. Risø National Laboratory.

Baracat, P. A. A., Rosolen, C. V. A. G., Carvalho, R. M., Ismail, K. A. R., Okita, W. M., Morais, T. N., & Carneiro, F. O. M. (2019). Comparative analysis of two airfoils for possible utilization in small wind turbines. In *Proceedings of the 25th ABCM International Congress of Mechanical Engineering*. https://doi.org/10.26678/ABCM.COBEM2019.COB2019-1762

Barlas, T. Pirrung, G. R., Ramos-García, N., Horcas, S. G., Mikkelsen, R. F., Olsen, A. S., & Gaunaa, M. (2021). Wind tunnel testing of a swept tip shape and comparison with multi-fidelity aerodynamic simulations. *Wind Energy Science, 6*, 1311-1324. https://doi.org/10.5194/wes-6-1311-2021

Burton, T., Sharpe, D., Jenkins, N., & Bossanyi, E. (2001). *Wind energy handbook*. John Wiley & Sons. https://doi.org/10.1002/0470846062

Canale, T., Ismail, K. A. R., & Lino, F. A. M. (2018). Aerodynamic evaluation of Gottingen and Joukowski airfoils for use in rotors of small wind turbines. In K. Cavalca, & H. Weber (Eds.), *Proceedings of the 10th International Conference on Rotor Dynamics–IFToMM. IFToMM 2018. Mechanisms and machine science, vol 63* (pp. 531-543). Springer. https://doi.org/10.1007/978-3-319-99272-3_37

Dorrell, J., & Lee, K. (2020). The cost of wind: Negative economic effects of global wind energy development. *Energies, 13*(14), Article 3667. https://doi.org/10.3390/en13143667

Drela, M. (2013). XFoil 6.99. *Massachusetts Institute of Technology*. https://web.mit.edu/drela/Public/web/xfoil/

Fadil, J., Soedibyo, & Ashari, M. (2017). Performance comparison of vertical axis and horizontal axis wind turbines to get optimum power output. In *Proceedings of the 15th International Conference on Quality in Research (QiR): International Symposium on Electrical and Computer Engineering* (pp. 429-433). https://doi.org/10.1109/QIR.2017.8168524

Fritz, E. K., Ferreira, C., & Boorsma, K. (2022). Na efficient blade sweep correction model for blade element momentum theory. *Wind Energy, 25*(12), 1977-1994. https://doi.org/10.1002/we.2778

Fritz, E., Boorsma, K., & Ferreira, C. (2024). Experimental analysis of a horizontal-axis wind turbine with swept blades using PIV data. *Wind Energy, 9*, 1617-1629. https://doi.org/10.5194/wes-9-1617-2024

Gemaque, M. L. A., Vaz, J. R. P., & Saavedra, O. R. (2022). Optimization of hydrokinetic swept blades. *Sustainability, 14*(21), Article 13968. https://doi.org/10.3390/su142113968

Gowda, A. S. (2019). Comparison of aerodynamic performance of NACA 4412 and 2412 using computational approach. *International Journal of Engineering Trends and Technology, 67*(4), 73-75. https://doi.org/10.14445/22315381/IJETT-V67I4P216

Gözcü, O., Kim, T., Verelst, D. R., & McWilliam, M. K. (2022). Swept blade dynamic investigations for a 100 kW small wind turbine. *Energies, 15*(9), 3005. https://doi.org/10.3390/en15093005

Hansen, M. O. L. (2008). *Aerodynamics of wind turbines*. Earthscan.

Hepperle, M. (2018). JavaFoil. *AeroTools*. http://www.mhaerotools.de/airfoils/javafoil.htm

Hernández, J. G. G., & Cabrera, R. S. (2018). Representation and estimation of the power coefficient in wind energy conversion systems. *Revista Facultad de Ingeniería, 28*(50), 70-90. https://doi.org/10.19053/01211129.v28.n50.2019.8816

Horcas, S. G., Ramos García, N., Li, A., Pirrung, G., & Barlas, T. (2023). Comparison of aerodynamic models for horizontal axis wind turbine blades accounting for curved shapes. *Wind Energy, 26*, 5-22. https://doi.org/10.1002/we.2780

Johari, M. K., Jalil, M. A. A., & Shariff, M. F. M. (2018). Comparison of horizontal axis wind turbine (HAWT) and vertical axis wind turbine (VAWT). *International Journal of Engineering and Technology, 7*(4.13), 74-80. https://doi.org/10.14419/ijet.v7i4.13.21333

Kamran, M. (2022). *Fundamentals of smart grid systems*. Academic Press. https://doi.org/10.1016/C2021-0-02193-3

Kaya, M. N., Kose, F., Ingham, D., Ma, L., & Pourkashanian, M. (2018). Aerodynamic performance of a horizontal axis wind turbine with forward and backward swept blades. *Journal of Wind Engineering & Industrial Aerodynamics, 176*, 166-173. https://doi.org/10.1016/j.jweia.2018.03.023

Khalafallah, M. G., Ahmed, A. M., & Emam, M. K. (2019). The effect of using winglets to enhance the performance of swept blades of a horizontal axis wind turbine. *Advances in Mechanical Engineering, 11*(9). https://doi.org/10.1177/1687814019878312

Khandakar, A., & Kashem, S. B. A. (2020). Feasibility study of horizontal axis wind turbine. *ARIV-International Journal of Technology, 1*(2), Article AIJT12092020.

Kulunk, E., & Yilmaz, N. (2009). HAWT rotor design and performance analysis. In *Proceeding of the ASME 3rd International Conference of Energy Sustainability*. https://doi.org/10.1115/ES2009-90441

Larwood, S., van Dam, C. P., & Schow, D. (2014). Design studies of swept wind turbine blades. *Renewable Energy, 71*, 563-571. https://doi.org/10.1016/j.renene.2014.05.050

Li, A., Gaunaa, M., Pirrung, G. R., Ramos García, N., & Horcas, S. G. (2020). The influence of the bound vortex on the aerodynamics of curved wind turbine blades. *Journal of Physics: Conference Series, 1618*, Article 052038. https://doi.org/10.1088/1742-6596/1618/5/052038

Li, A., Pirrung, R., Gaunaa, M., Madsen, H. A., & Horcas, S. G. (2022). A computationally efficient engineering aerodynamic model for swept wind turbine blades. *Wind Energy Science, 7*, 129-160. https://doi.org/10.5194/wes-7-129-2022

Liu, J., Lin, H., & Zhang, J. (2019). Review on the technical perspectives and commercial viability of vertical axis wind turbines. *Ocean Engineering, 182*, 608-626. https://doi.org/10.1016/j.oceaneng.2019.04.086

Liu, S., & Janajreh, I. (2012). Development and application of an improved blade element momentum method model on horizontal axis wind turbines. *International Journal of Energy and Environmental Engineering, 3*, Article 30. https://doi.org/10.1186/2251-6832-3-30

Manwell, J. F., McGowan, J. G., & Rogers, A. L. (2009). *Wind energy explained*. John Wiley & Sons. https://doi.org/10.1002/9781119994367

Otero, A. D., & Ponta, F. L. (2018). On the sources of cyclic loads in horizontal-axis wind turbines: The role of blade-section misalignment. *Renewable Energy, 117*, 275-286. https://doi.org/10.1016/j.renene.2017.10.049

Pavese, C., Tibaldi, C., Zahle, F., & Kim, T. (2017). Aeroelastic multidisciplinary design optimization of a swept wind turbine blade. *Wind Energy, 20*, 1941-1953. https://doi.org/10.1002/we.2131

Pholdee, N., Kumar, S., Bureerat, S., Nuantong, W., Dongbang, W. (2023). Sweep blade design of an axial wind turbine using a surrogate-assisted differential evolution algorithm. *Journal of Applied and Computational Mechanics, 9*(1), 217-225. https://doi.org/10.22055/jacm.2022.40974.3682

Redchyts, D., Portal Porras, K., Tarasov, S., Moiseienko, S., Tuchyna, U., Starun, N., & Fernandez Gamiz, U. (2023). Aerodynamic performance of vertical axis wind turbines. *Journal of Marine Science and Engineering, 11*(7), Article 1367. https://doi.org/10.3390/jmse11071367

Roy, S., Das, B., & Biswas, A. (2021). Influence of chamber ratio and thickness ratio on the airfoil performance. In K. M. Pandey, R. D. Misra, P. K. Patowari, & U. S. Dixit (Eds.), *Recent advances in mechanical engineering. Lecture notes in mechanical engineering* (pp. 729-737). Springer. https://doi.org/10.1007/978-981-15-7711-6_72

Scott, S., Capuzzi, M., Langstan, D., Bossanyi, E., McCann, G., Weaver, P. M., Pirrera, A. (2017). Effects of aeroelastic tailoring on performance characteristics of wind turbine systems. *Renewable Energy, 114*, 887-903. https://doi.org/10.1016/j.renene.2017.06.048

Sessarego, M., Ramos García, N., & Shen, W. Z. (2018). Analysis of winglets and sweep on wind turbine blades using a lifting line vortex particle method in complex inflow conditions. *Journal of Physics: Conference Series, 1037*, Article 022021. https://doi.org/10.1088/1742-6596/1037/2/022021

Sharma, V., Sharma, S., & Sharma, G. (2022). Recent development in the field of wind turbine. *Materials Today: Proceedings, 64*, 1512-1520. https://doi.org/10.1016/j.matpr.2022.05.459

Somers, D. M. (1997). *Design and experimental results for the S809 airfoil*. National Renewable Energy Laboratory. https://doi.org/10.2172/437668

Veloso, M. J. G., Santos, C. H. P., Vaz, J. R. P., & Neto, A. M. C. (2023). Quasi-steady analysis of a small wind rotor with swept blades. *Sustainability, 15*(13), Article 10211. https://doi.org/10.3390/su151310211

Verelst, D. R. S., & Larsen, T. J. (2010). Load consequences when sweeping blades–A case study of a 5 MW pitch controlled wind turbine. *DTU Research Database*. https://orbit.dtu.dk/files/4610035/ris-r-1724.pdf

Wiser, R., & Millstein, D. (2020). Evaluating the economic return to public wind energy research and development in the United States. *Applied Energy, 261*, Article 11449. https://doi.org/10.1016/j.apenergy.2019.114449